Toward Accurate Physics-Based Specifications of Neutral Density using GNSS-Enabled Small Satellites

Eric K. Sutton[1], Jeffrey P. Thayer[1,2], Marcin D. Pilinski[3], Shaylah M. Mutschler[2], Thomas E. Berger[1], Vu Nguyen[4], Dallas Masters[4]

[1]Space Weather Technology, Research and Education Center (SWx TREC), University of Colorado at Boulder.

[2]Ann and H.J. Smead Aerospace Engineering Sciences, University of Colorado at Boulder.

[3]Laboratory for Atmospheric and Space Physics (LASP), University of Colorado at Boulder.

[4]Spire Global, Inc., Boulder, CO.

Corresponding author: Eric Sutton (eric.sutton@colorado.edu)

Key Points:

- GNSS-enabled satellites are capable of monitoring the state of the thermosphere at much higher cadences than current operational datasets
- We present an initial technique to infer neutral densities from orbit determination products of the Spire CubeSat constellation
- Densities are used to drive a data-assimilative, physics-based model of the thermosphere and ionosphere during 23 Sept.–9 Dec. 2018

Abstract

Satellite-atmosphere interactions cause large uncertainties in low-Earth orbit determination and prediction. Thus, knowledge of and the ability to predict the space environment, most notably thermospheric mass density, are essential for operating satellites in this domain. Recent progress has been made toward supplanting the existing empirical, operational methods with physics-based data-assimilative models by accounting for the complex relationship between external drivers such as solar irradiance, Joule, and particle heating, and their response in the upper atmosphere. Simultaneously, a new era of CubeSat constellations is set to provide data with which to calibrate our upper-atmosphere models at higher spatial resolution and temporal cadence. With this in mind, we provide an initial method for converting precision orbit determination (POD) solutions from global navigation satellite system (GNSS) enabled CubeSats into timeseries of thermospheric mass density. This information is then fused with a physics-based, data-assimilative technique to provide calibrated model densities.

Plain Language Summary:

Satellites with heights below 1,000 kilometers (or about 600 miles) travel through the upper atmosphere, which influences the path of their orbits. This influence has been monitored, in some capacity, since the first man-made orbiting satellites were launched into space, but predicting the effects is still quite difficult. Now commercial satellite “mega constellations” are being launched into the region at a fast pace, which means that all satellite paths must be known and projected into the future with great accuracy in order to avoid high-speed collisions. Using Global Positioning System (GPS) signals, this work blends information from tracking the position of the mega-constellation satellites themselves with a high-fidelity model of the upper atmosphere, in an attempt to improve our knowledge of where satellites are and where they are going to be.

1 Introduction

Within low-Earth orbit (LEO), a region spanning roughly 100 to 1000 km in altitude for the purposes of this paper, interactions between man-made satellites and the ambient atmosphere cause large uncertainties in the orbit determination and prediction processes (Berger et al., 2020). During episodic periods of moderate to severe space weather activity, such atmospheric drag

uncertainties can amplify by a factor of 2–5 in a matter of minutes to hours (Krauss et al., 2015; Sutton et al., 2005). These uncertainties, when combined with the steadily growing launch rate of small satellites and CubeSats and our advancing ability to track smaller and smaller objects, are poised to overwhelm the U.S. Department of Defense infrastructure currently carrying out the Detect–Track–Catalog mission. Products of this mission are pervasive across the Space Situational Awareness (SSA) and Space Traffic Management (STM) enterprises and form a critical infrastructure for nearly all space-based activities. Thus, knowledge and prediction of the space environment, particularly the neutral mass density of the thermosphere and lower exosphere, are an essential part of satellite operations within LEO.

One of the major obstacles in predicting orbit trajectories hours to days in advance, and in correlating consecutive or irregular object tracking data with a particular orbiting object, comes from the legacy framework used to model the upper atmosphere's state and its interaction with satellites and debris. The current model employed by the Combined Space Operations Center (CSpOC) and is the High Accuracy Satellite Drag Model (HASDM) (Storz et al., 2005), an empirical model that self-calibrates by ingesting ground-based tracking data of a select set of orbiting "calibration objects"—i.e., operational and defunct satellites passing through LEO with reasonably stable ballistic coefficients. While this method provides an accurate global-average snapshot of the upper atmosphere, its abilities to capture realistic spatial structure and forecast into the future are limited, particularly ahead of geomagnetic storming that has the largest impact on LEO orbital tracking. Physics-based upper atmosphere simulation approaches offer a vast potential improvement in this regard. Models in this category solve a set of Navier-Stokes fluid equations that have been appropriately tailored for use in the upper atmosphere and are therefore inherently better equipped for simulating a dynamic system response to impulsive energy input from the solar wind and coronal mass ejections. For years the computational cost of these models prohibited their use in an operational setting. However, present-day computing technology is abundantly capable of running an ensemble of such models in near real time. Instead, the primary reason that physics-based methods remain to be adopted by operational centers is the lack of robust data assimilation schemes capable of self-calibrating at levels equal to or better than those currently used in combination with empirical models.

Fortunately, significant strides have been made in recent years toward supplanting empirical methods with physics-based data assimilative models of the upper atmosphere. One

such advancement has been accomplished by accounting for the complex relationship between external drivers—namely solar flux, Joule, and particle heating—and the response of the upper atmosphere by employing a new least-squares filter called the Iterative Driver Estimation and Assimilation (IDEA) technique (Sutton, 2018). The new filter operates similarly to an unscented Kalman filter (UKF) with the addition of mechanisms to accommodate the lagged response of the upper atmosphere to variations in the external drivers. Using this new technique, notable improvements in neutral density specification—even during a geomagnetic storm—have already been demonstrated (Sutton, 2018), which can help to lower the uncertainty of orbit determination and prediction across the LEO catalog, thereby increasing the efficacy of STM activities, including satellite conjunction assessment and collision avoidance. In addition, the emergence of large constellations of commercial and academic CubeSats over the past 5 years brings with it an excellent opportunity. Most newer SmallSats and CubeSats are equipped with Global Navigation Satellite System (GNSS) devices, making them valuable sources of Precision Orbit Determination (POD) information. Many are also equipped with the ability to monitor their attitude, allowing the construction of an accurate force model. This information can be combined to initialize and constrain models of the upper atmosphere.

In order to track the state of the upper atmosphere with reasonable fidelity, the HASDM model ingests observations from ground-based radar tracks of known objects using a similar technique to the one we present here. However, in order to make strides in specifying and predicting the state of the thermosphere, new data sets with increased spatial resolution, temporal cadence, and global coverage are needed (Bruinsma, Fedrizzi, et al., 2021). Satellite-based GNSS observations are capable of describing the space environment at a much higher spatial resolution and temporal cadence. Whereas the conventional radar-derived, satellite-drag data sets operate on a multi-orbit to multi-day cadence, we will show that the GNSS-derived data sets are capable of operating at a cadence of a single orbital period, i.e., on the order of hours rather than days. Even higher cadences may also be possible but will require further development. The remainder of the paper details our efforts to use the new set of information provided by CubeSats to drive a physics-based, data-assimilative approach to simulating atmospheric densities in LEO.

2 Datasets

2.1 Spire CubeSats

Spire operates a constellation of over 100 CubeSats in LEO with altitudes ranging from 400–650 km and inclinations spanning the globe, from equatorial to polar orbits. Figure 1 gives a snapshot of the distribution of altitude and orbit inclination of Spire CubeSats as of late January 2021.

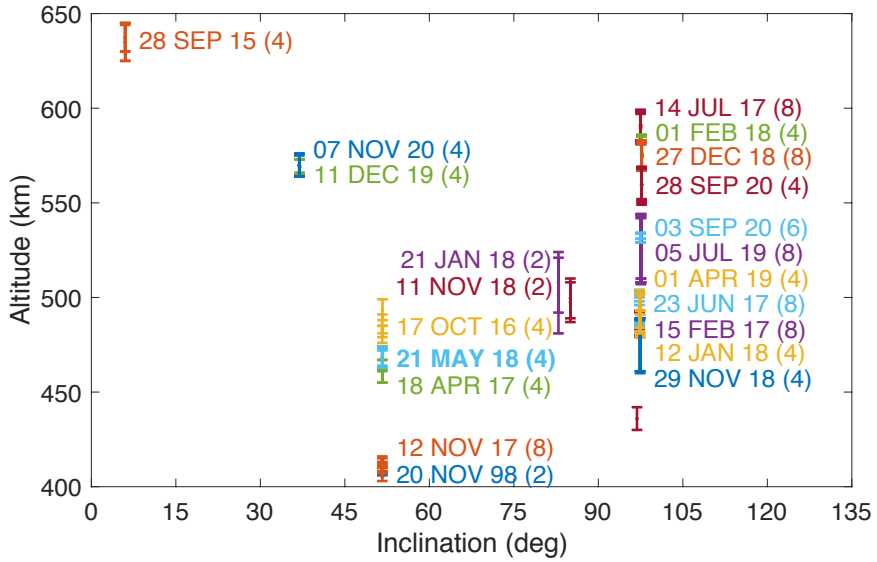

Figure 1. Current coverage of altitude versus inclination for the Spire constellation of CubeSats (as of 26 January 2021). The error bars show the perigee-to-apogee range of altitudes. CubeSats are color coded by common launch dates with the total number of CubeSats in each launch group indicated in parentheses. The 21 May 2018 launch date is emphasized to indicate the launch date of the three satellites used in this study.

The data sets used in this study were provided by Spire Global as part of the NASA Commercial SmallSat Data Pilot Program and cover the period of 23 Sept.–9 Dec. 2018. For the purposes of our work, the following data products were utilized:

- POD solution ephemeris derived from GNSS tracking
- Satellite pointing in the form of attitude quaternions
- Satellite geometry model

125 POD solutions were typically available during the duty cycle of the GNSS/Radio
126 Occultation (RO) instrument. For the 2018 dataset, duty cycles were in the range of 30–40% of
127 the time, usually concentrated along 40- to 60-minute segments of an orbit (referred to hereafter
128 as an orbit arc). This efficiency has increased with more recent CubeSat builds such that current
129 duty cycles are beginning to approach 100%. For the current data set, ephemeris from each orbit
130 arc were estimated using the RTOrb software (https://gps-
131 solutions.com/brochures/GPSS_Brochure_RTOrb_ Nov_2011.pdf). This software implements a
132 Kalman filter-based approach to estimate orbit ephemeris. As configured for the current dataset,
133 RTOrb considers Earth's gravity up to degree and order 120 from the EIGEN-2 model (Reigber
134 et al., 2003), Luni-Solar 3rd body perturbations, atmospheric drag assuming densities from the
135 Mass Spectrometer Incoherent Scatter extension (MSISe-90) model (Hedin, 1991), and solar
136 radiation pressure (SRP) with cylindrical Earth-shadowing effects. The latter two effects use a
137 cannonball approach in which coefficients of drag and reflectivity are estimated within each arc,
138 respectively, along with the orbit ephemeris. The treatment of drag and SRP in the POD process
139 is not to be confused with the force model described later in this section; instead, the parameters
140 estimated here have little bearing on our calculations of orbit energy.

141 The attitude of the Spire CubeSats is represented by a quaternion describing the
142 transformation from the body-fixed coordinate system (see Figure 4 below) to the vehicle
143 velocity/local horizontal (VVLH) orbit-based coordinate system at a given instance in time.
144 These data enable the orientation of the satellite with respect to the final coordinate system
145 introduced in Section 3.2. In the initial phases of the NASA Data Pilot assessment, quaternions
146 were provided at an approximate cadence of 10 seconds during the duty cycle of the GNSS/RO
147 receiver, with nothing available outside of the duty cycle. However, it was realized early on in
148 the project that, due to frequent orientation maneuvers, the accuracy of the retrieved neutral
149 densities would be limited by any breaks in continuity of satellite attitude data (see Section 3.3
150 for further details). The attitude mode of the CubeSats frequently switched between an observing
151 mode aligning GNSS/RO antennas along track and a mode that maximizes the amount of solar
152 flux incident on the solar panels. Because these changes in orientation modify the integrated
153 effect that atmospheric drag has on the orbit parameters, the orientation must be monitored
154 constantly in order to convert orbital energy loss rates to an atmospheric density. Spire has since
155 updated their processing chain for the entire fleet to ensure that a continuous stream of attitude

quaternions is available for any datasets originating after 2018. However, for the 2018 data set, processing was limited to a small subset of three CubeSats from Spire Global's constellation for which attitude data had been continuously downlinked and archived. These satellites, which will be used throughout the remainder of the paper, are referred to by Spire's internal satellite ID numbers: 83, 84, and 85. These three CubeSats trace back to a common launch on 21 May 2018 into a 51.6° inclination orbit. During the time period of interest these satellites orbited between the altitudes of 467–492 km and remained within 800–2100 km (or 2–4.5 minutes) of one another along the orbit track. Additional properties and designations of these CubeSats can be found in Table 1.

Table 1. Properties of Spire CubeSats used in this study. Note: the last three columns apply to all three satellites

Spire ID	NORAD ID	COSPAR ID	Perigee/Apogee Altitude (km)	Inclination (degrees)	S/C Mass (g)
83	43560	2018-046G			
84	43559	2018-046F	467–492	51.6	4933 ± 4
85	43558	2018-046E			

Figure 2 shows the geometry for the three Spire CubeSats. The GNSS/POD antenna nominally points in the zenith direction while the front radio occultation (FRO) antenna generally points along the in-track or anti-in-track directions when the satellite is recording RO data. When the RO instrument is cycled off, the satellite reorients in such a way as to maximize illumination of the solar panels.

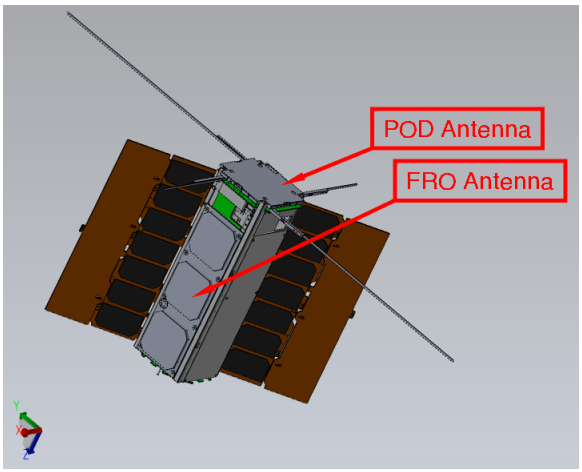

Figure 2. Computer model of Spire's version 3.3 Lemur CubeSat.

2.2 Swarm Satellite Mission

As an independent data source, neutral densities from the Swarm satellite mission (Friis-Christensen et al., 2008) are used to compare with the assimilated model density output at locations that differ from the Spire dataset. Anomalies in the Swarm accelerometer data were noticed early in the mission (Siemes et al., 2016), preventing their use for neutral density determination using established methods (e.g., Bruinsma et al., 2004; Doornbos et al., 2010; Sutton et al., 2007). Instead, GNSS tracking data are used to produce POD solutions of neutral density for the Swarm satellites at a temporal resolution of about 20 minutes, which is then used to constrain the uncertainties in the accelerometer measuremens (van den IJssel et al., 2020).

The Swarm mission consists of three satellites: Swarm-A, -B, and -C. Swarm-A and -C reside in essentially the same near-polar orbit, while the orbit of Swarm-B is higher in altitude and slightly lower in inclination. Of the three satellites, accelerometer data is only currently available from Swarm-C. This data, referred to as Swarm-C ACC, spans the altitude range of 437–468 km during the 2018 period of interest. During this period, anomalies in the data can cause the densities to attain non-physical values; these are removed from data prior to performing any comparison. In addition, orbital averages of the Swarm-C densities are taken and compared with a corresponding orbital average of model densities in order to mitigate any spurious errors in the accelerometer data. The orbital plane of Swarm-C precesses 12 hours with respect to local time approximately every 133 days of the mission. Because the lower-inclination Spire CubeSats precess much faster (i.e., 12 hours of local-time precession every 31.25 days),

194 Swarm-C data allows us to assess the accuracy of the assimilation model for local times and
195 locations far away from the ingested Spire data over the 2018 period of interest.

196 **3 Methods**

197 3.1 Orbital Energy Determination

198 To drive our data assimilative process, we use information from GNSS measurements
199 taken aboard CubeSats. There are several methods available to infer neutral densities from orbit
200 positioning information. For instance, this can be done by estimating a scaling correction for a
201 density model within a POD solution using two-line element (TLE, e.g., Brandt et al., 2020) sets
202 or GNSS tracking (e.g., van den IJssel & Visser, 2007) . We choose instead to employ a model-
203 agnostic energy tracking method that uses the existing POD solutions routinely obtained by
204 Spire. The first step is to calculate the orbital energy at each available ephemeris data point and
205 track the change in this quantity between subsequent orbits. For an Earth-orbiting satellite, this
206 energy can be approximated in the following way:

207 $$\xi = \frac{v^2}{2} - \omega_{Earth}^2 \frac{x^2+y^2}{2} - \frac{\mu}{r} - U_{nonSpherical} \quad (1)$$

208 where $r = \sqrt{x^2 + y^2 + z^2}$ and v are the satellite's respective position and velocity in an Earth-
209 centered Earth-fixed (ECEF) coordinate frame, ω_{Earth} is the rotation rate of the Earth, μ is the
210 gravitational parameter for the Earth, and $U_{nonSpherical}$ is a potential function describing
211 deviations in Earth's gravitational field from the purely spherical (i.e., $-\mu/r$) term. $U_{nonSpherical}$
212 is most commonly expressed as a spherical harmonic expansion of degree, n, and order, m. In
213 the absence of nonconservative forces (e.g., atmospheric drag or solar radiation pressure) or any
214 additional perturbing conservative forces not accounted for in Equation 1 (e.g., 3rd body
215 attraction, solid Earth tides, ocean tides, atmospheric tides, etc.), ξ is a conserved quantity along
216 the orbit of a satellite.

217 We have found that the choice of Earth-fixed coordinates becomes important when
218 considering the non-spherical gravity terms in the energy equation (i.e., Equation 1), particularly
219 any non-zonal terms (i.e., $m > 0$), which depend on longitude. In ECEF coordinates,
220 $U_{nonSpherical}$ is clearly a function of position alone. The alternate formulation of the energy
221 equation in an inertial coordinate frame, however, would require $U_{nonSpherical}$ to be a function

of both position and time, violating the assumptions underlying a potential function and its use in the energy equation. As a result, the formulation of energy in an inertial coordinate frame does not remain constant along an orbit when considering non-zonal terms—even in the absence of nonconservative forces—and leads to twice-daily oscillations of approximately ±130–140 J/kg/s or m^2/s^3 for the orbits analyzed in this paper, or equivalently, about ±30–35 m in the semi-major axis. Much of this can be directly attributed to the $n = m = 2$ gravitational potential term, which is the largest non-zonal term in $U_{nonSpherical}$. The 3rd body attraction from the sun and moon depend on time in both Earth-fixed or inertial coordinates, although much less so in the latter. While fairly minor, the work done by 3rd body attraction on a satellite's orbit can be taken into account over time using the following equation:

$$\Delta\xi_{3B} = \int_{t_0}^{t_1} \vec{a}_{3B}(\vec{r}, t) \cdot \vec{v}\, dt \tag{2}$$

where $\Delta\xi_{3B}$ is the difference in orbital energy due to 3rd body acceleration between times t_0 and t_1; $\vec{r}$ and $\vec{v}$ are the position and velocity vectors in ECEF coordinates; and $\vec{a}_{3B}$ is the acceleration vector of the satellite caused by the gravitational attraction from the sun and moon, also expressed in the ECEF reference frame. In contrast to Equation 1, continuous knowledge of the satellite ephemeris is required in order to carry out the integral calculation of Equation 2. While this is not available directly from the GNSS measurements due to duty cycling, it can be obtained at sufficient precision using Two-Line Element (TLE) sets along with the Simplified General Perturbations (SGP4) satellite propagator, both available at https://space-track.org. The continuous position of the sun and moon were obtained from JPL's planetary and lunar ephemeris product (Park et al., 2021 and references therein).

If we describe the Earth's gravity field using the two-body approximation—ignoring for a moment the non-spherical and 3rd body contributions—the energy dissipation due to atmospheric drag remains obscured by the large variations in energy due to Earth's J_2 oblateness term (i.e., $n = 2, m = 0$) and higher-order gravitational terms. The light blue data points in Figure 3 show this simplified calculation of orbital energy for a single CubeSat from Spire Global's constellation (satellite 83) during the period spanning 23 Sept.–9 Dec. 2018. However, when we account for a spherical harmonic gravity field up to degree and order 36 and 3rd body effects, the change in energy caused by atmospheric drag is more readily isolated from variations in the gravity field as depicted by the dark blue curve.

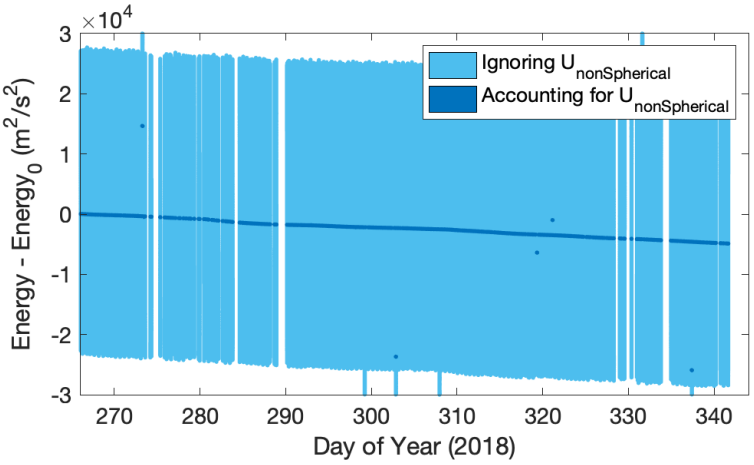

Figure 3. Keplerian orbital energy (light blue curve, i.e., ignoring the $U_{nonSpherical}$ term from Equation 1) and total orbital energy (dark blue curve, i.e., including the $U_{nonSpherical}$ term from Equation 1) for Spire CubeSat 83 during the period of 23 Sept.–9 Dec. 2018.

Figure 4 depicts the orbital energy of all three CubeSats over the same time span as Figure 3 but zoomed in to reveal variations in the rate of decay. To conform with the POD solutions, we have used the non-spherical terms specified by the EIGEN-2 gravity model (Reigber et al., 2003). We found that, for our purposes, including terms of degree or order higher than 36 yielded diminishing returns.

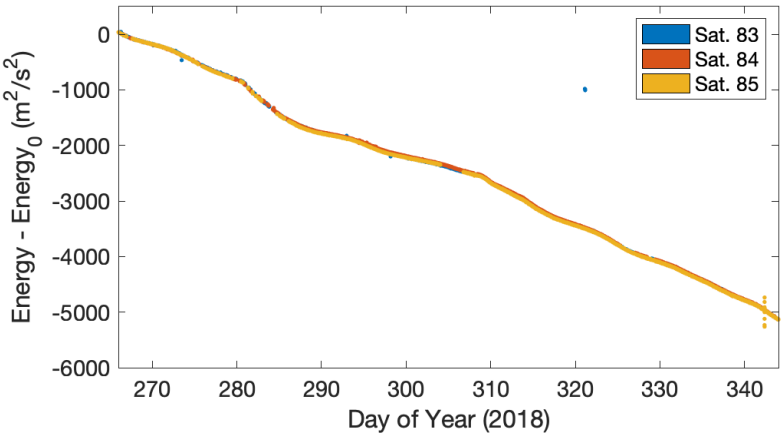

Figure 4. Orbital energy (i.e., including the $U_{nonSpherical}$ term from Equation 1) for Spire CubeSats 83, 84, and 85 during the period of 23 Sept.–9 Dec. 2018. The three timeseries lie approximately on top of one another, given that they reside in nearly the same orbit and therefore experience very similar accelerations.

During this period of time, the energy curves track one another quite well due, in part, to the fact that all three CubeSats occupy essentially the same orbital plane, with separations along the orbit track in the range of 800–2100 km (or 2–4.5 minutes). Changes in energy were on the order of 5000 m^2/s^2 over the entire period of analysis, or about 65 m^2/s^2 per day. This is equivalent to a change in the semi-major axis of 1.2 km total, or about 15 meters per day. These magnitudes are specific to the size, shape and ballistic coefficients of the satellites, as well as the altitude and prevailing geophysical conditions sampled during the time period of interest. After applying a simple filter to reject erroneous arcs (note the obvious outliers on day 273, 320, and 342 in Figure 4), the noise level of these timeseries of orbital energy becomes low enough to derive an effective energy dissipation rate between subsequent orbit arcs.

3.2 Satellite Force Model

To interpret the timeseries of energy from Figure 4 in terms of the behavior of the upper atmosphere, it is necessary to understand how the satellite drag interaction depends on atmospheric density. The rate at which energy is lost from a satellite's orbit to the atmosphere via the drag force, or the energy dissipation rate (EDR), can be related to atmospheric mass density through the following equation:

$$EDR \equiv -\frac{d\xi}{dt} = \frac{1}{2m} C_D A_{ref} \rho v^3 \quad (3)$$

where C_D is the satellite's coefficient of drag, A_{ref} is the cross-sectional area of the satellite projected in the direction of v, the velocity of the satellite in the ECEF coordinate frame, m is the satellite mass, ρ is the mass density. Winds are neglected in this equation, however, the co-rotation of the atmosphere with the Earth is automatically considered through the use of ECEF coordinates. The force model of Sutton (2009) is used to compute the coefficient of drag. From their Equation 7, we consider the transfer of momentum between incoming atmospheric particles and the satellite surface assuming that particles are accommodated to the approximate surface temperature of the satellite using an accommodation coefficient of $\alpha = 0.93$. While the accommodation coefficient is kept constant, both C_D and A_{ref} can vary significantly over the course of an orbit due to changes in the attitude of the satellite.

In order to compare two subsequent observations of orbital energy ξ_0 and ξ_1 calculated by Equations 1 and 2 at their respective epochs t_0 and t_1, Equation 3 can be integrated to find the dependence on atmospheric density:

$$\xi_1 - \xi_0 = -\frac{1}{2m} \int_{t_0}^{t_1} C_D A_{ref} \rho v^3 dt = -\frac{1}{2m} \rho_{eff} \int_{t_0}^{t_1} C_D A_{ref} v^3 dt \quad (4)$$

Solving for ρ_{eff}, similar in theme to the work of Picone (2005), gives an effective mass density between t_0 and t_1 along the orbit of the satellite.

Figure 5 shows the simulated change in orbital energy normalized by neutral density (EDR/ρ) as given by Equation 3 for one of Spire Global's CubeSats according to its orientation over the course of a single day. This parameter, which we can refer to simply as the force model, is the conversion factor between the observed energy dissipation rate and atmospheric density. The periodic shift between pointing modes—one optimized for RO sensing and the other for solar panel illumination—can be clearly seen in Figure 5. Accounting for the large variations in the force model becomes crucial because a satellite can dwell in a given pointing mode for a significant fraction of an orbit, and this dwell time is not necessarily consistent between orbits. If neglected, these approximate factor-of-two variations in the force model have the potential of causing errors of similar magnitude in the density retrievals.

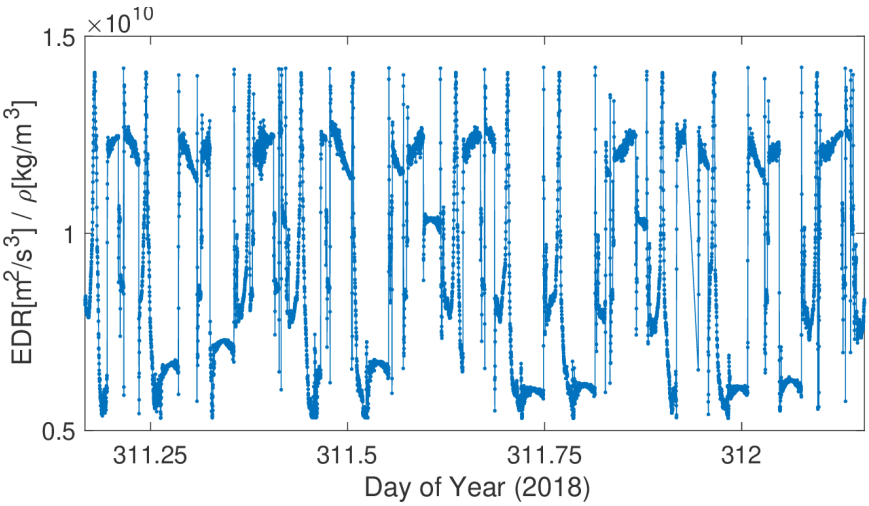

Figure 5. Force model for Spire CubeSat 83 for a single day starting early on 7 Nov. The force model is the conversion factor between the observed energy dissipation rate and atmospheric density.

3.3 Data Assimilation

After processing the GNSS measurements and applying the force model described above, the final step in our process is to ingest these observations into a data assimilative framework to correct the global upper atmospheric density. Here we briefly describe the Iterative Driver Estimation and Assimilation (IDEA) technique, based on the method of Sutton (2018). This method accounts for the complex relationship between external drivers—namely solar flux and geomagnetic heating—and the resulting response of the upper atmosphere. In general, these drivers are poorly monitored and often rely on proxies that only very approximately represent the physical mechanisms that heat and energize the upper atmosphere. To represent the absorption of solar extreme and far ultraviolet (EUV/FUV) irradiance, the solar radio flux at 10.7 cm wavelength ($F_{10.7}$) is often used as a proxy. In terms of the solar wind–magnetosphere–ionosphere–thermosphere interaction, the geomagnetic Kp index is often used to characterize heating and momentum exchange at high latitudes. Empirical formulas, such as the Heelis et al. (1982) convection electric field model, are then used to help convert these proxies into atmospheric heating, incurring further uncertainty into the overall modeling process. The reliance on these proxies and their empirical coupling functions leads to large uncertainties when driving a model of the thermosphere.

IDEA estimates corrections to the external forcing parameters and their empirical coupling functions in order to bring a physics-based model into better agreement with direct observations of the thermosphere. The discrepancies between model output and observations are minimized by employing a least-squares filter similar in nature to an unscented Kalman filter (UKF). Figure 6 compares the IDEA process (right) to that of a typical ensemble Kalman filter (EnKF) configured for ionosphere/thermosphere modeling. IDEA runs several versions of the thermosphere model, each experiencing slightly different external driving conditions.

In the current implementation of IDEA, the Thermosphere–Ionosphere–Electrodynamics General Circulation Model (TIEGCM) (Qian et al., 2014; Richmond et al., 1992; Sutton et al., 2015) is used as the physics-based environment model. TIEGCM is a finite-difference solution to the conservation equations of momentum, mass, and energy describing the upper atmosphere in the presence of momentum and energy sources. TIEGCM accounts for the dominant features in the upper atmosphere of molecular diffusion and circulation, solar heating in the EUV and FUV bands, and high-latitude auroral heating. TIEGCM also has the ability to simulate the ionosphere and associated electrodynamic coupling between the neutral and plasma environment in a self-consistent manner at middle and low latitudes. The model spans from 97 km at its lower boundary to between 450 and 700 km at its upper boundary, mostly depending on the level of solar flux. Migrating diurnal and semi-diurnal tides are specified at the lower boundary in a climatological sense. Other dynamic features of the lower and middle atmosphere are ignored, which could lead to uncertainty when estimating corrections to the external forcing.

In terms of data assimilation, additional measures must be taken to deal with the lagged response of the upper atmosphere to variations in the external drivers. It is well known that the response of the thermosphere can take on a large range of timescales depending on several factors, height being among the largest contributors. In order for an estimated correction of the external forcing parameters to have a timely effect on the model, the time-lagged response must be accounted for. IDEA abandons the sequential filtering techniques typically used for ionosphere/thermosphere applications (e.g., M. V. Codrescu et al., 2004, 2021; S. M. Codrescu et al., 2018; Fuller-Rowell et al., 2004; Godinez et al., 2015; Matsuo et al., 2012, 2013; Minter et al., 2004; Morozov et al., 2013; Murray et al., 2015). Instead, an iterative approach is adopted so that estimated forcing parameters can be re-applied to a simulation over the course of a day so

that the model can respond to forcing (refer to the additional feedback loop on the right side of Figure 6).

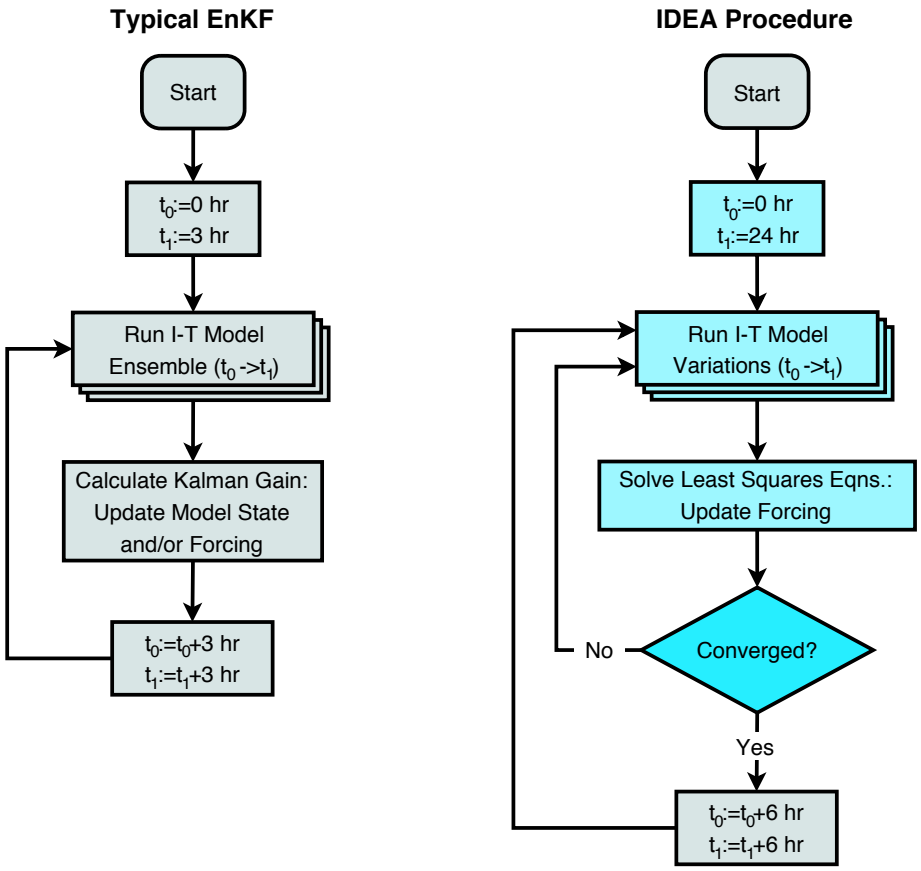

Figure 6. Comparison of a typical Ensemble Kalman Filter as configured for use with a time-dependent thermospheric model (left) with the IDEA technique (right; features in color differ from their counterparts in the EnKF flow chart on the left), where t_0 and t_1 are the respective start and end times of the model runs during a given data assimilation cycle (adapted from Sutton, 2018).

In Sutton (2018), satellite-borne accelerometer observations of thermosphere density were used to calibrate the external forcing parameters driving the TIEGCM. Here we use EDRs based on POD ephemeris derived from GNSS measurements from 3 satellites from Spire Global's constellation of CubeSats. A forward model, based on output from the TIEGCM, the satellite geometry model shown in Figure 2, and the force model of Sutton (2009), is used to synthesize orbital energy dissipation for each satellite according to Equation 4. Accelerometer instruments operate at high cadence (0.1–1 Hz) equating to a resolution of 7–70 km along the

satellite's orbit. The GNSS/POD data set yields a measurement of density more on the order of once per orbit arc (possibly higher with additional development). This difference in information content between data sets necessitates additional consideration when designing a thermospheric estimation filter. In this case, we found that the observability of IDEA was limited to estimation of the most recent daily $F_{10.7}$ value and the most recent 6-hourly effective Kp value for each assimilation cycle. The configuration used in this study iterates 3 times per assimilation cycle and uses five 48-core nodes of a high-performance computer (HPC) to advance by 6 hours to the next assimilation cycle in less than 3 minutes (i.e., >120x realtime). For comparison, Sutton (2018) found it possible to estimate the most recent daily $F_{10.7}$ value and the three most recent 3-hourly Kp values for each assimilation cycle when using the high-resolution accelerometer-derived density data set. However, it is expected that improvements in observability will be enabled through the use of more CubeSats in the estimation process. And considering the greater coverage of CubeSats in altitude and local time, accuracy could very well exceed accelerometer-based density model corrections.

4 Results and Discussion

The period spanning 23 Sept.–9 Dec. 2018 (days 266–343) of our study was marked with very low activity in terms of the magnitude and variation of solar EUV and FUV, as approximated by measurements of the 10.7 cm solar radio flux ($F_{10.7}$; top panel of Figure 7). Note that $F_{10.7}$ has an approximate lower bound of 66 solar flux units (sfu) at solar minimum and attains values above 200 during solar maximum. During the latter, 27-day solar rotational modulation can also produce large swings in $F_{10.7}$, causing large signals in the thermospheric density. Because the available data for this studyfalls firmly within solar minimum, the variations seen here are quite small. In terms of geomagnetic activity, however, there were two minor-to-moderate disturbances on 7 Oct. (day 280) and 4 Nov. (day 308) as shown by the 3-hourly Kp geomagnetic index (lower panel of Figure 7).

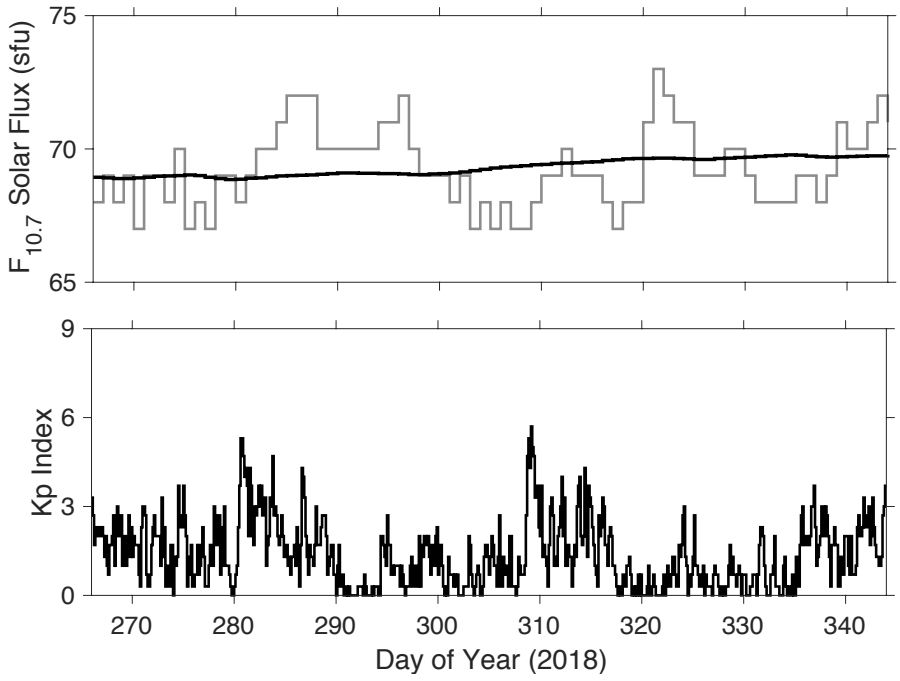

Figure 7. Top: observed solar $F_{10.7}$ radio flux. The grey curve is the daily measured value from the Ottawa observatory normalized to 1 AU sun-earth distance; the black curve is an 81-day (~3 solar rotation) centered average. Bottom: the 3-hourly planetary magnetic index Kp. Both panels span the period of interest 23 Sept.–9 Dec. 2018.

Given observations of orbital variations and an appropriate force model as discussed in the previous section, an effective atmospheric mass density can be inferred between consecutive orbit arcs. Figure 8 shows such neutral mass densities derived from the three CubeSats (blue, red and yellow curves) of Spire's constellation. The cadence of these densities is approximately one measurement for each consecutive set of orbit arcs. For the time period studied, this equates to a cadence of about 2–2.5 hours on average. This cadence depends on the instrument duty cycle, which has steadily improved since 2018. A higher cadence may be possible in the future as duty cycle improves, however, the exact allowable cadence will also depend on the altitude of the satellite and the noise errors of the GNSS measurements. HASDM output is also shown with the black curve for reference. This empirical model is calibrated by ground-based radar tracking observations of approximately 70–90 orbiting objects. Because the individual tracking observations are sparse—relative to those available from GNSS—densities derived from this technique have an effective cadence of several hours to several days (Storz et al., 2005).

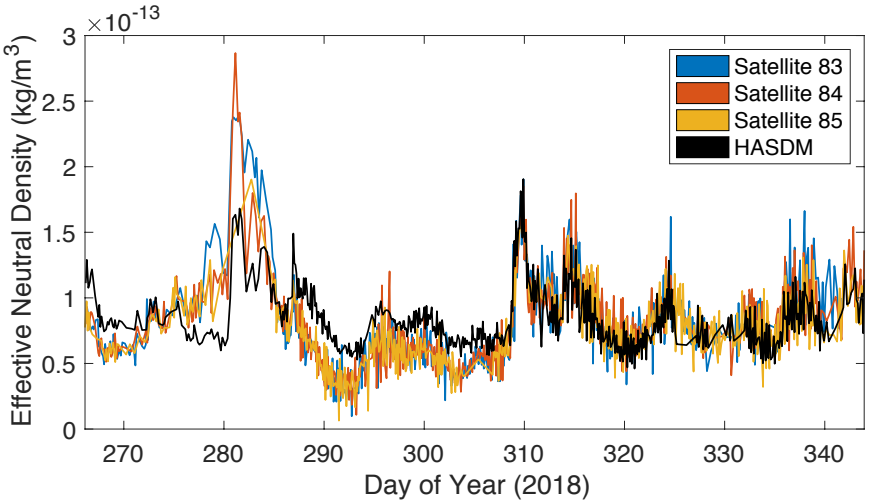

Figure 8. Neutral mass densities derived from Spire CubeSats 83–85. Also shown is output from HASDM as sampled on the orbit of satellite 84. The values plotted are the effective densities (see the right-hand side of Equation 4) between subsequent orbit arcs.

The CubeSat-derived densities maintain good agreement with one another, given the close proximity of all three spire satellites within 800–2100 km (or 2–4.5 minutes) along the orbit track. Agreement with HASDM is also reasonable during this time period. As Figure 7 shows, there are several minor to moderate variations in Kp over the time interval. The signatures of these disturbances are also seen in the neutral densities of Figure 8. There are several deviations between data and model though, most notably around days 270, 290, and 300, where CubeSat-derived densities are significantly lower than HASDM. We have not yet concluded whether model or data are in error during these intervals, since very little ground-truth data exists during this period for validation. Another period of discrepancy exists around the geomagnetic disturbance on day 280, where CubeSat-derived densities experience a much larger storm-time increase. While it is possible that the higher cadence GNSS densities are capturing actual storm dynamics better than HASDM, we note that POD data were less frequent during this particular event than during other times. Additionally, attitude data was unavailable for satellite 83 over much of the disturbance, particularly days 282–285. The discrepancy in amplitude during this event could also be a function of the higher cadence of the CubeSat POD data fit spans (5–6 hours during this event) relative to that of the HASDM data fit spans (~1 day or more), in which case, the CubeSat-derived densities would be expected to more accurately resolve the storm-time disturbance.

441 In general, some error in the observations and modeled output is expected, of
442 instrumental, data sampling, and geophysical origins. Part of this error is caused by variations in
443 sampling location for a given data point. In other words, the data points presented in Figure 8 do
444 not represent the density averaged over a complete orbit; instead, each data point can be sampled
445 over a very different part of the globe than the previous. The resulting error can be seen in the
446 HASDM model, which if plotted as an average over full orbits, would appear much more
447 smooth. Another important source of error in the density timeseries comes directly from
448 uncertainties in the POD solutions themselves. Because the POD solutions were not designed
449 with a thermospheric application in mind, we expect that some of the estimation parameters may
450 have been overfit. And finally, there is certainly an amount of geophysical variability seen in the
451 observed density timeseries that is not captured by the HASDM model. While an in-depth error
452 analysis is beyond the scope of the present work, we will continue to investigate techniques to
453 minimize these sources of error, including improving the underlying POD solutions and
454 combining timeseries from additional satellites.

455 A central goal of this work is to ingest multiple data sources into a physics-based,
456 assimilative thermosphere model to combine information and mitigate the uncertainty of any one
457 dataset. Figure 9 shows the baseline TIEGCM simulation without any assimilation (grey curve)
458 driven externally by the observed geophysical indices (GPI) of Kp and $F_{10.7}$; the POD-based
459 densities derived using the techniques described in the previous Section (blue, red, and yellow
460 curves); and the IDEA output over the interval spanning 23 Sept.–9 Dec. 2018 (solid black
461 curves).

462 The baseline TIEGCM-GPI simulation shows muted response to the Kp and $F_{10.7}$ inputs
463 during this solar-minimum interval, when compared with the IDEA output (or with the HASDM
464 output in Figure 8). CubeSat densities and IDEA output agree very well over the interval. There
465 are, however, several short periods when POD data from a single satellite becomes sparse, such
466 as the period around day 304–306 for satellite 85 (yellow curve), or when attitude data becomes
467 unavailable, such as the period around day 282–285 for satellite 83 (blue curve). There are also
468 several periods during which data from a single satellite becomes spurious, not agreeing with the
469 data from the other two satellites, such as the period around 335–340 for satellite 85 (yellow
470 curve). In these cases, the other two data sets tend to compensate for missing or spurious data
471 from the third satellite. This leads us to believe that adding data from additional satellites and

constellations should improve performance and increase the "signal-to-noise ratio" of the data assimilation process.

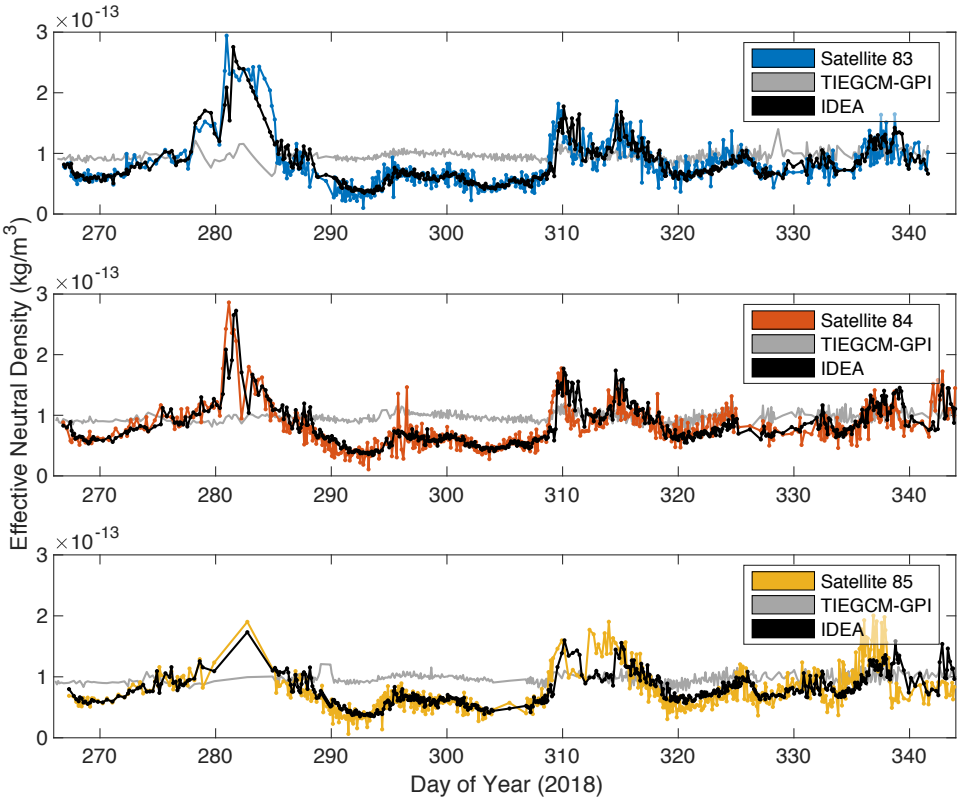

Figure 9. Comparison of observations with model output. CubeSat-derived densities are given by the colored curves for satellites 83 (top), 84 (middle), and 85 (bottom). Also shown is the output from the baseline thermosphere model driven by measured geophysical indices (TIEGCM-GPI, grey curves) $F_{10.7}$ and Kp. The data assimilation IDEA output is given along each of the CubeSat orbits by the black curves.

The performance of these models with respect to the CubeSat-derived densities are assessed using the metrics of Sutton (2018) and Bruinsma, Boniface, et al. (2021). These consist of the mean (μ), standard deviation (σ), and root mean square error ($RMSe$) of the ratio of model density to observed density, all computed in logarithmic space:

$$\mu(m/o) = \exp\left(\frac{1}{N}\sum_{i=1}^{N} \ln\frac{\rho_{m,i}}{\rho_{o,i}}\right) \quad (5)$$

$$\sigma(m/o) = \sqrt{\frac{1}{N}\sum_{i=1}^{N}\left(\ln\frac{\rho_{m,i}}{\rho_{o,i}} - \ln\mu(m/o)\right)^2} \quad (6)$$

$$RMSe(m/o) = \sqrt{\frac{1}{N}\sum_{i=1}^{N}\left(\ln\frac{\rho_{m,i}}{\rho_{o,i}}\right)^2} \quad (7)$$

As mentioned in Sutton (2018), these metrics have several properties that are desirable when working with the ratio of two quantities that vary exponentially, such as neutral densities. The $RMSe(m/o)$ and $\sigma(m/o)$ quantities are best interpreted as a percentage in the following way: $\% = 100 \times (\exp\sigma(m/o) - 1)$. The $RMSe(m/o)$ is a combination of $\mu(m/o)$ and $\sigma(m/o)$, as can be see through the following relation: $RMSe(m/o)^2 = (\ln\mu(m/o))^2 + \sigma(m/o)^2$. The $RMSe(m/o)$ is therefore a good indicator of total model errors. However, if the intent is to drive a POD process using the density model, it may be more informative to use the $\sigma(m/o)$ metric, since a ballistic coefficient is typically estimated per satellite. In practice, this estimated ballistic coefficient will soak up errors not only in the assumed coefficient of drag, but also in the mean bias of the density model. Table 2 shows the overall performance of the three models, TIEGCM-GPI, HASDM, and IDEA at re-creating the energy dissipation rates observed by the Spire CubeSats' GNSS data. Table 2 also shows the performance of the three models in synthesizing the independent data set of orbit-averaged neutral densities from the Swarm-C satellite.

During the period of interest, the IDEA method outperforms HASDM in all three metrics with respect to the assimilated Spire data. This is true of both the prior and posterior IDEA estimates of density. The 'posterior' IDEA estimate is the fully assimilated nowcast solution, whereas the 'prior' IDEA estimate is a 6-hour forward simulation (i.e., forecast) by the TIEGCM based on the initial conditions and estimated drivers from the previous posterior assimilation cycle. The prior mean is expected to remain close to the posterior mean if no major changes in the actual geophysical conditions occur during this 6-hour span. Minor fluctuations in the actual conditions could cause upward or downward trends over a given 6-hour span, resulting in density variations that tend to average out of $\mu(m/o)$ while slightly increasing the $\sigma(m/o)$ metric for the prior IDEA estimates relative to the posterior. It should be noted, however, that IDEA has a clear advantage in this comparison over the other two models, since IDEA assimilates the very

data that it is now being compared against. This comparison confirms that the IDEA technique, as an estimation filter, has the requisite control authority to sufficiently adjust the model to the assimilated data set.

To go a step further, the Swarm-C ACC data is used as an independent data source to assess the performance of IDEA in locations outside the vicinity of assimilated data. Due to the differences in precession rates between the Spire CubeSats and the Swarm-C satellite, the local times of their orbital planes align approximately once every 41 days. This alignment occurs twice during the 23 Sept.–9 Dec. 2018 time period, on 10 Oct. (day 283) and 20 Nov. (day 324). Aside from these brief alignment periods lasting only a few days, Spire and Swarm data sets are sampling vastly different sectors of the globe. Table 2 shows that IDEA succeeds in reducing the $\mu(m/o)$ and overall $RMSe(m/o)$ with respect to the free-running TIEGCM-GPI simulation but at the expense of an increased $\sigma(m/o)$. In the comparison with Swarm-C data, HASDM performs the best in all three metrics. However, it should be noted that HASDM has a clear advantage in this comparison over the other models because HASDM assimilates data from ~75 satellites from across the globe while IDEA only assimilates within a single orbit.

Sutton (2018) used accelerometer-derived neutral densities from a single satellite to drive the IDEA technique. In the previous study, the technique showed high proficiency for estimating neutral densities in local times away from where the assimilated data resided. In the current work, using effective neutral densities from a single orbit plane at an approximate 2–2.5 hour cadence per satellite, the comparison with data from other local times deteriorates. While this is not all that surprising, it does provide some insight into the specificity required to apply adequate corrections to the external drivers. The observability of these corrections depends on features of the observations, including the global coverage, spatial resolution, temporal cadence, measurement error, and measurement type (e.g., mass density from accelerometers vs. chemical composition from a mass spectrometer). In essence, the impact that each external driver has on the observation must be distinguishable from the impact caused by other drivers. With accelerometer data, this is satisfied to some extent because measurements are of high cadence and sample two distinct local time and all latitudes over the course of an orbit. Any change in geomagnetic activity will first impact high-latitude thermosphere before influencing lower latitudes, while changes in solar flux affect the thermosphere in a much less localized manner. Likewise, the model's day-to-night ratio of density will decrease as geomagnetic activity

increases yet is only slightly affected by variations in solar flux (Waldron, 2020). Both of these signals can be discerned with accelerometer data but not with orbit-averaged data. Several questions remain: Can this issue of observability with POD-inferred densities be overcome by including data from multiple local-time orbital planes and/or with reduced averaging? And in terms of assimilation, which characteristic of a density data set is more valuable, spatial resolution in the latitudinal direction or sampling of multiple local time planes?

Table 2. Performance metrics of each model with respect to the assimilated Spire Global CubeSat data and independent Swarm-C ACC data, calculated over the entire interval spanning days 266–343, 2018. Orbital averages of the Swarm-C data (as well as the corresponding model output) have been taken to minimize the effect of spurious errors in the accelerometer data.

	TIEGCM-GPI	HASDM	IDEA	
			Prior	Posterior
Assimilated Spire CubeSat POD Data				
$\mu(m/o)$	1.33	1.10	1.04	1.04
$\sigma(m/o)$	48.7%	40.6%	34.6%	30.7%
$RMSe(m/o)$	62.7%	42.6%	34.9%	31.1%
Independent Swarm-C ACC Orbit-Averaged Data				
$\mu(m/o)$	1.40	1.12	1.20	1.19
$\sigma(m/o)$	24.9%	8.2%	37.2%	32.4%
$RMSe(m/o)$	49.6%	15.2%	43.8%	39.4%

5 Summary and Conclusions

The increases in satellite and debris populations in LEO necessitates improvements in how we detect, track, and catalog orbiting objects. Additionally, if we are to avoid catastrophic collisions in LEO, we must also be able to reliably predict the trajectories of satellites multiple days in advance, giving satellite operators sufficient lead time to plan safe and effective maneuvers. With the variability of the space environment, particularly thermospheric mass density, being the largest uncertainty in the orbit prediction chain, this study investigates new ways to monitor the upper atmosphere. In this notoriously data-starved region, the instrumentation commonly carried on recently launched LEO SmallSats and CubeSats,

particularly GNSS receivers, can be used to improve the accuracy of physics-based neutral density specifications. Notably, the amount of data available from this new category of observation should continue to scale with the crowdedness of LEO, whereas the current ground-based tracking database remains limited in quantity and resolution.

In the current work, we have applied a post-processing method to the timeseries of POD ephemeris from three CubeSats in Spire's constellation. This has allowed us to track the time evolution of orbital energy of each CubeSat over an orbit arc. Further application of a satellite-surface force model converts this information into a timeseries of *in situ* atmospheric mass density. By analyzing 78 days' worth of data from late 2018, we were able to observe the impact of minor and moderate fluctuations in geomagnetic activity during the prevailing solar minimum conditions. We also found good agreement with HASDM, one of the only sources of thermospheric data currently available for comparison. While the resulting timeseries from a single satellite may be prone to errors, identified here simply as a discrepancy between density timeseries derived from co-orbiting CubeSats, this can be mitigated by assimilating timeseries from multiple data sets into a physics-based model of the thermosphere.

Additionally, with more advanced processing methods, it may be possible to lower the error for timeseries of individual CubeSats. The POD solutions used here were not specifically tailored to the application of measuring density. One potential complication is that overfitting of parameters or insufficient arc size may have led to significant noise in the inferred densities. Future work will focus on improving the POD solutions to reduce error and finding the optimal size of the POD fitting window as a function of altitude, phase of the solar cycle, satellite geometry characteristics, and GNSS instrument precision and errors. With these improvements in place, it may even be possible to attain higher cadences than a single data point per orbit. This has been demonstrated when using a state-of-the-art geodetic GNSS receiver (van den IJssel & Visser, 2007), but extending this technique to GNSS-equipped SmallSat constellations would provide much needed global coverage of thermospheric observations. When paired with a suitable assimilative, physics-based models of the thermosphere, there is great potential to lower the uncertainty of orbit predictions across the LEO catalog, improve the accuracy of conjunction assessments, and increase the efficacy of STM activities.

Acknowledgments

EKS, JPT, and TEB acknowledge the generous support of the University of Colorado at Boulder Grand Challenge Grant: Space Weather Technology, Research, and Education Center (SWx TREC). EKS gratefully acknowledges support from the NASA Operations-to-Research (O2R) program under grant number 80NSSC20K1399. Support for SMM has been provided by the National Defense Science and Engineering Graduate (NDSEG) Fellowship program. Data from the Spire constellation used in this study may be requested and downloaded from the NASA Commercial SmallSat Data Acquisition Program (CSDAP) website at https://earthdata.nasa.gov/esds/csdap. The TIEGCM is developed and maintained by the National Center for Atmospheric Research's High Altitude Observatory (HAO) and is available at https://www.hao.ucar.edu/modeling/tgcm/tie.php. The HASDM density data are provided for scientific use courtesy of Space Environment Technologies (SET) and can be downloaded from https://spacewx.com/hasdm/. Swarm-C ACC data is available from ESA at https://swarm-diss.eo.esa.int/#swarm/Level2daily/Entire_mission_data/DNS/ACC/Sat_C. The TLE sets and the SGP4 satellite propagator are available at https://space-track.org. Planetary and lunar ephemeris are available from the JPL Solar System Dynamics website at https://ssd.jpl.nasa.gov/.

References

Berger, T. E., Holzinger, M. J., Sutton, E. K., & Thayer, J. P. (2020). Flying Through Uncertainty. *Space Weather*, *18*(1), 1–5. https://doi.org/10.1029/2019SW002373

Brandt, D. A., Bussy-Virat, C. D., & Ridley, A. J. (2020). A Simple Method for Correcting Empirical Model Densities During Geomagnetic Storms Using Satellite Orbit Data. *Space Weather*, *18*(12). https://doi.org/10.1029/2020SW002565

Bruinsma, S., Tamagnan, D., & Biancale, R. (2004). Atmospheric densities derived from CHAMP/STAR accelerometer observations. *Planetary and Space Science*, *52*(4), 297–312. https://doi.org/10.1016/j.pss.2003.11.004

Bruinsma, Sean, Fedrizzi, M., Yue, J., Siemes, C., & Lemmens, S. (2021). Charting Satellite Courses in a Crowded Thermosphere. *Eos*, *102*. https://doi.org/10.1029/2021EO153475

Bruinsma, Sean, Boniface, C., Sutton, E. K., & Fedrizzi, M. (2021). Thermosphere modeling capabilities assessment: geomagnetic storms. *Journal of Space Weather and Space Climate*,

11, 12. https://doi.org/10.1051/swsc/2021002

Codrescu, M. V., Fuller-Rowell, T. J., & Minter, C. F. (2004). An ensemble-type Kalman filter for neutral thermospheric composition during geomagnetic storms. *Space Weather*, *2*(11). https://doi.org/10.1029/2004SW000088

Codrescu, M. V., Codrescu, S. M., & Fedrizzi, M. (2021). Storm Time Data Assimilation in the Thermosphere Ionosphere with TIDA. *Submitted to Space Weather*. https://doi.org/10.1002/essoar.10505945.1

Codrescu, S. M., Codrescu, M. V., & Fedrizzi, M. (2018). An Ensemble Kalman Filter for the Thermosphere-Ionosphere. *Space Weather*, *16*(1), 57–68. https://doi.org/10.1002/2017SW001752

Doornbos, E., van den IJssel, J., Luhr, H., Forster, M., & Koppenwallner, G. (2010). Neutral Density and Crosswind Determination from Arbitrarily Oriented Multiaxis Accelerometers on Satellites. *Journal of Spacecraft and Rockets*, *47*(4), 580–589. https://doi.org/10.2514/1.48114

Friis-Christensen, E., Lühr, H., Knudsen, D., & Haagmans, R. (2008). Swarm – An Earth Observation Mission investigating Geospace. *Advances in Space Research*, *41*(1), 210–216. https://doi.org/10.1016/j.asr.2006.10.008

Fuller-Rowell, T. J., Minter, C. F., & Codrescu, M. V. (2004). Data assimilation for neutral thermospheric species during geomagnetic storms. *Radio Science*, *39*(1). https://doi.org/10.1029/2002RS002835

Godinez, H. C., Lawrence, E., Higdon, D., Ridley, A., Koller, J., & Klimenko, A. (2015). Specification of the Ionosphere-Thermosphere Using the Ensemble Kalman Filter (pp. 274–283). https://doi.org/10.1007/978-3-319-25138-7_25

Hedin, A. E. (1991). Extension of the MSIS Thermosphere Model into the middle and lower atmosphere. *Journal of Geophysical Research: Space Physics*, *96*(A2), 1159–1172. https://doi.org/10.1029/90JA02125

Heelis, R. A., Lowell, J. K., & Spiro, R. W. (1982). A model of the high-latitude ionospheric convection pattern. *Journal of Geophysical Research*, *87*(A8), 6339. https://doi.org/10.1029/JA087iA08p06339

van den IJssel, J., & Visser, P. (2007). Performance of GPS-based accelerometry: CHAMP and GRACE. *Advances in Space Research*, *39*(10), 1597–1603. https://doi.org/10.1016/j.asr.2006.12.027

van den IJssel, J., Doornbos, E., Iorfida, E., March, G., Siemes, C., & Montenbruck, O. (2020). Thermosphere densities derived from Swarm GPS observations. *Advances in Space Research*, *65*(7), 1758–1771. https://doi.org/10.1016/j.asr.2020.01.004

Krauss, S., Temmer, M., Veronig, A., Baur, O., & Lammer, H. (2015). Thermospheric and geomagnetic responses to interplanetary coronal mass ejections observed by ACE and GRACE: Statistical results. *Journal of Geophysical Research: Space Physics*, *120*(10), 8848–8860. https://doi.org/10.1002/2015JA021702

Matsuo, T., Fedrizzi, M., Fuller-Rowell, T. J., & Codrescu, M. V. (2012). Data assimilation of thermospheric mass density. *Space Weather*, *10*(5). https://doi.org/10.1029/2012SW000773

Matsuo, T., Lee, I.-T., & Anderson, J. L. (2013). Thermospheric mass density specification using an ensemble Kalman filter. *Journal of Geophysical Research: Space Physics*, *118*(3), 1339–1350. https://doi.org/10.1002/jgra.50162

Minter, C. F., Fuller-Rowell, T. J., & Codrescu, M. V. (2004). Estimating the state of the thermospheric composition using Kalman filtering. *Space Weather*, *2*(4). https://doi.org/10.1029/2003SW000006

Morozov, A. V., Ridley, A. J., Bernstein, D. S., Collins, N., Hoar, T. J., & Anderson, J. L. (2013). Data assimilation and driver estimation for the Global Ionosphere–Thermosphere Model using the Ensemble Adjustment Kalman Filter. *Journal of Atmospheric and Solar-Terrestrial Physics*, *104*, 126–136. https://doi.org/10.1016/j.jastp.2013.08.016

Murray, S. A., Henley, E. M., Jackson, D. R., & Bruinsma, S. L. (2015). Assessing the performance of thermospheric modeling with data assimilation throughout solar cycles 23 and 24. *Space Weather*, *13*(4), 220–232. https://doi.org/10.1002/2015SW001163

Park, R. S., Folkner, W. M., Williams, J. G., & Boggs, D. H. (2021). The JPL Planetary and Lunar Ephemerides DE440 and DE441. *The Astronomical Journal*, *161*(3), 105. https://doi.org/10.3847/1538-3881/abd414

Picone, J. M. (2005). Thermospheric densities derived from spacecraft orbits: Accurate

processing of two-line element sets. *Journal of Geophysical Research*, *110*(A3), A03301. https://doi.org/10.1029/2004JA010585

Qian, L., Burns, A. G., Emery, B. A., Foster, B., Lu, G., Maute, A., et al. (2014). The NCAR TIE-GCM: A Community Model of the Coupled Thermosphere/Ionosphere System. In *Modeling the Ionosphere-Thermosphere System* (Vol. 9780875904, pp. 73–83). https://doi.org/10.1002/9781118704417.ch7

Reigber, C., Schwintzer, P., Neumayer, K.-H., Barthelmes, F., König, R., Förste, C., et al. (2003). The CHAMP-only earth gravity field model EIGEN-2. *Advances in Space Research*, *31*(8), 1883–1888. https://doi.org/10.1016/S0273-1177(03)00162-5

Richmond, A. D., Ridley, E. C., & Roble, R. G. (1992). A thermosphere/ionosphere general circulation model with coupled electrodynamics. *Geophysical Research Letters*, *19*(6), 601–604. https://doi.org/10.1029/92GL00401

Siemes, C., de Teixeira da Encarnação, J., Doornbos, E., van den IJssel, J., Kraus, J., Pereštý, R., et al. (2016). Swarm accelerometer data processing from raw accelerations to thermospheric neutral densities. *Earth, Planets and Space*, *68*(1), 92. https://doi.org/10.1186/s40623-016-0474-5

Storz, M. F., Bowman, B. R., Branson, M. J. I., Casali, S. J., & Tobiska, W. K. (2005). High accuracy satellite drag model (HASDM). *Advances in Space Research*, *36*(12), 2497–2505. https://doi.org/10.1016/j.asr.2004.02.020

Sutton, E. K. (2009). Normalized Force Coefficients for Satellites with Elongated Shapes. *Journal of Spacecraft and Rockets*, *46*(1), 112–116. https://doi.org/10.2514/1.40940

Sutton, E. K. (2018). A New Method of Physics-Based Data Assimilation for the Quiet and Disturbed Thermosphere. *Space Weather*, *16*(6), 736–753. https://doi.org/10.1002/2017SW001785

Sutton, E. K., Forbes, J. M., & Nerem, R. S. (2005). Global thermospheric neutral density and wind response to the severe 2003 geomagnetic storms from CHAMP accelerometer data. *Journal of Geophysical Research: Space Physics*, *110*(A9). https://doi.org/10.1029/2004JA010985

Sutton, E. K., Thayer, J. P., Wang, W., Solomon, S. C., Liu, X., & Foster, B. T. (2015). A self-

consistent model of helium in the thermosphere. *Journal of Geophysical Research: Space Physics*, *120*(8), 6884–6900. https://doi.org/10.1002/2015JA021223

Sutton, Eric K., Nerem, R. S., & Forbes, J. M. (2007). Density and Winds in the Thermosphere Deduced from Accelerometer Data. *Journal of Spacecraft and Rockets*, *44*(6), 1210–1219. https://doi.org/10.2514/1.28641

Waldron, Z. C. (2020). *Investigation of the Day-to-Night Ratio in the Thermosphere Mass Density* (master's thesis). University of Colorado Boulder. Retrieved from https://scholar.colorado.edu/concern/graduate_thesis_or_dissertations/w6634477g